A New Approach to Aflatoxin Detection in Chili Pepper by Machine Vision

M. Ataş*, Y. Yardimci, A. Temizel

Graduate School of Informatics,
Middle East Technical University, Ankara, Turkey
* Corresponding author: M. Ataş, e-mail: hakmesyo@gmail.com

Abstract

Aflatoxins are the toxic metabolites of Aspergillus molds, especially by Aspergillus flavus and Aspergillus parasiticus. They have been studied extensively because of being associated with various chronic and acute diseases especially immunosuppression and cancer. Aflatoxin occurrence is influenced by certain environmental conditions such as drought seasons and agronomic practices. Chili pepper may also be contaminated by aflatoxins during harvesting, production and storage. Aflatoxin detection based on chemical methods is fairly accurate. However, they are time consuming, expensive and destructive. We use hyperspectral imaging as an alternative for detection of such contaminants in a rapid and nondestructive manner. In order to classify aflatoxin contaminated chili peppers from uncontaminated ones, a compact machine vision system based on hyperspectral imaging and machine learning is proposed. In this study, both UV and Halogen excitations are used. Energy values of individual spectral bands and also difference images of consecutive spectral bands were utilized as feature vectors. Another set of features were extracted from those features by applying quantization on the histogram of the images. Significant features were selected based on proposed method of hierarchical bottleneck backward elimination (HBBE), Guyon's SVM-RFE, classical Fisher discrimination power and Principal Component Analysis (PCA). Multi layer perceptrons (MLP) and linear discriminant analysis (LDA) were used as the classifiers. It was observed that with the proposed features and selection methods, robust and

higher classification performance was achieved with fewer numbers of spectral bands enabling the design of simpler machine vision systems.

Keywords: Machine vision, aflatoxin detection, hyperspectral imaging, food safety, feature extraction, feature subset selection, classification, multi layer perceptron.

1. INTRODUCTION

Aflatoxins are toxic compounds produced by many species of Aspergillus molds, especially by Aspergillus flavus and Aspergillus parasiticus (Zeringue et al, 1998). The term "aflatoxin" comes from Aspergillus flavustoxin. As International Agency for Research on Cancer (IARC) pointed out, aflatoxin causes human liver cancer (IARC, 2002). A wide variety of foods (hazelnut, pistachio nut, almond, dried fig, wheat, corn, chili pepper, etc...) are susceptible to aflatoxin contamination that degrades food quality and threatens human health. Therefore, several countries have taken strict regulations to control aflatoxin contamination level. Generally accepted aflatoxin level in food is, 20 ppb (parts per billion) in both USA and Turkey. On the other hand maximum level of aflatoxin B1 and total aflatoxin was determined as 5 ppb and 10 ppb in European countries, respectively (Commission Regulation [EC], 2006).

Aflatoxin contamination can occur during pre-harvesting and post-harvesting periods. High temperature, prolonged drought conditions and high insect activities are significant factors for aflatoxin contamination during pre-harvesting. For post-harvesting, warm temperature and high humidity factors become active ingredients that increase the mold invasion and toxin production

(Wagacha and Muthomi, 2008). High Performance Liquid Chromatography (HPLC), Mass Spectroscopy (MS), Thin Layer Chromatography (TLC), and Enzyme-Linked Immunosorbent Assay (ELISA) are widely known chemical aflatoxin detection methods amongst which HPLC is superior in terms of accuracy and sensitivity (Chen et al, 2005). As an alternative to chemical methods, machine vision and pattern classification techniques are considered for aflatoxin detection because they are faster, cheaper and nondestructive (Kalkan et al., 2011, Yao et al., 2011, Yao et al., 2006, Pearson et al., 2001). As Shotwell et al. (1972), Fersaie et al. (1978), Doster et. al, 1998 and Herrman, (2002) pointed out, under ultraviolet 365 nm illumination, aflatoxin contaminated samples exhibit bright green yellowish fluorescence (BGYF). However it should be noted that the mechanism is much more complex. Certain fungi produce kojic acid which may result in BGYF when there is enough peroxidase enzyme in the plant. It is known that not all fungi that produce kojic acid also produce aflatoxins. Similarly, the lack of peroxidase enzyme may conceal the presence of aflatoxins because BGYF will be absent. Thus, BGYF itself does not directly indicate the actual presence of aflatoxin and it may result in false positives and negatives during the evaluation stage. Furthermore, in the previous studies on corn and pistachio the authors (Pearson et al., 2001, Yao et al., 2006) stated that BGYF phenomenon under UV illumination is observed when average aflatoxin level exceeds 100 ppb. Therefore, BGYF based aflatoxin detection is not always recommended (Fersaie et al, 1978, Herrman, 2002, Doster et. al, 1998). Some researchers used BGYF in their studies. Utilizing the reflectance ratios of 440/490nm and 450/490 nm, Tyson and Clark, (1974) achieved 90% classification rate by examining aflatoxin-infected pecans under UV fluorescence. By analyzing corn kernels, again Yao et al. (2006) achieved 87% and 88% classification performance for 20 ppb and 100 ppb aflatoxin level thresholds. Kalkan et al. (2011) studied hazelnuts and red chili peppers and achieved 92.3% and 79.2% classification accuracies respectively. Another possible excitation mode is halogen illumination. Hirano et al. (1998) used transmittance ratio (T700nm/ T1100 nm) bands for peanuts classification under halogen illumination and achieved 95% classification accuracy. Pearson et al. (2001) achieved 96.6% classification accuracy rate of corn samples illuminated by 100W quartz-tungsten-halogen lamp by utilizing the spectral reflectance ratio (R735nm/R1005nm). They used discriminant analysis technique for detecting highly contaminated corn kernels (>100 ppb) from low contaminated (<10 ppb) or uncontaminated ones.

We consider aflatoxin detection in ground red chili pepper flakes in the present paper. The following section will describe hyperspectral data acquisition and preprocessing. Next, we will express our proposed feature extraction and selection approaches. Experimental results will be reported and discussed in Section 4. Finally in Section 5, we will give concluding remarks.

2. HYPERSPECTRAL IMAGE ACQUISITION AND PREPROCESSING

In the previous studies (Kalkan et al. 2011, Yao et al., 2006, Pearson et al., 2001), single illumination sources were used. More specifically, some studies were performed only under halogen illumination whereas others were done under UV. Basically, UV illumination is utilized for the fluorescence, halogen excitation is for reflectance phenomena. In order to investigate the contribution of those illuminations on the classifier performance, we utilized both excitations in this study. Figure 1 and Figure 2 depict a general overview of the hyperspectral imaging system and a flowchart and interrelated components of the proposed system, respectively.

Figure 1. A general overview of the hyperspectral imaging system

Totally 53 ground red chili pepper flake samples were gathered from different regions in Turkey. Most of them were sold as unpackaged. Figure 3 shows their aflatoxin variations as a histogram graph. Here we applied log10(1+Aflatoxin value) transformation in order to build a more compact histogram plot. As 10 ppb is the upper threshold for aflatoxin for spices and herbs in the EU (Commission Regulation [EC], 2006) we used 10 ppb as a threshold to classify the pepper samples into aflatoxin positive (contaminated) and negative (uncontaminated) groups. Mean aflatoxin level was measured as 16.78 ppb. Average aflatoxin levels for Afl- and Afl+ groups are 3.2 ppb and 33.3 ppb, respectively. As previous studies (Pearson et al., 2001, Yao et al., 2006) stated that BGYF is observed when aflatoxin level in the sample is high, we expect halogen illumination to contribute more for detection of aflatoxin for our chili pepper problem.

Figure 2. Flowchart and interrelated components of the proposed system.

The hardware of the image acquisition system is composed of a FireWire Sony CCD camera with Varispec liquid crystal tunable filter assembly. Hyperspectral image series ranging from 400 nm to 720 nm (10 nm spectral bandwidth) of 53 different chili pepper samples have been acquired under 100W quartz-tungsten-halogen and UV 365 nm illumination sources. Resolution of each image is 1280 X 960 pixels. During the acquisition process the set up was stationary, so there was no need to register the hyperspectral images. Images of three different locations of the same chili pepper sample were obtained in order to increase the training data. This also enables us to analyze a wider surface of the chili pepper sample. Figure 4 depicts sample images from the hyperspectral image series of uncontaminated and contaminated peppers for halogen and UV illuminations.

Figure 4. Sample images from the hyperspectral image series of uncontaminated and contaminated peppers for halogen and UV illuminations.

All the pepper samples were sent to TUBITAK Ankara Testing and Analyses Laboratory (ATAL) for HPLC analysis. Chili pepper samples that exceed 10 ppb threshold were labeled as aflatoxin positive otherwise they were labeled as aflatoxin negative for inductive learning.

Camera software by default applies histogram equalization to acquired images. Although, histogram equalization automatically controls oversaturation and under-saturation by applying adaptively changing exposure time, it also modifies original pixel values. To overcome this particular problem, one should fix the exposure time value of the camera and camera gain parameter to a predefined value. On the other hand, single exposure time eventually leads to under saturated and over saturated regions in the hyperspectral image series. Therefore, we dictated three spectral regions by manually changing exposure time values. Table 1 depicts the prescribed spectral regions, exposure times and corresponding normalization coefficients. We normalized the exposure of the images by their normalization coefficient before extracting the feature vectors. It should be noted that, exposure normalization leads some pixel values to exceed 255 pixel gray values and increase the dynamic range excessively. Therefore, we applied non-linear square root transformation in order to limit the range of the pixel value of the normalized images to 0-255 pixel gray value interval. With a maximum normalization coefficient of 9, a pixel value of 255 will yield corresponding maximum pixel gray value of 48 after the square root transformation. We used 48 levels to represent pixel gray values.

Table 1. Exposure normalization coefficients of the most informative regions of the spectral bands.

In order to eliminate the dust particles and reduce sensor noise in the images we applied 3x3 median filtering.

3. FEATURE EXTRACTION AND SELECTION

Classifier performance is strongly related to the relevance of the extracted features. In the ideal case, the feature vector should keep the most compact description of the desired function. In our problem this is the aflatoxin presence signature. Nevertheless, extracting meaningful and discriminative feature vector is not a straightforward and trivial process. It requires acquiring domain knowledge and underlying physical phenomena. In the hyperspectral images of chili pepper samples, shape and orientation of chili pepper flakes does not correlate with aflatoxin presence. Therefore, useful features should have weak relevance to the second order features like edges and orientation. Relying on solely spectral band mean intensity is not desirable either. There may be Afl- samples and Afl+ samples with nearly the same mean intensity value. In the previous studies, Kalkan et al., (2011) used wavelet based intensity features and achieved 79.2 % classification performance indicating that spatial and textural information contributes the prediction accuracy. Conversely, most of the researchers (Pearson et al, 2001, Yao et al. 2006, Hirano et al, 1998) utilized spectral band energies as a feature vector in their studies and achieve reasonable accuracy rates. In this study, we extracted features by applying histogram based feature extraction technique. Histogram based feature extraction was used in several studies Sakthivel et al (2010) used histogram based features for face recognition problem, Singh et al (2009) utilized histogram features for detecting insect damages in wheat kernels, ElMasry et al. (2007) used for detection of apple bruise and Yang et al. (2010) employed histogram features for food recognition. We will compare the performance of different types of features.

Another concern is the size of extracted feature vector. Larger feature size results in the well known "curse of dimensionality" problem. Increasing the feature vector dimension requires an exponential increase in the data size. Hence, the size of the feature vector should be reduced to an acceptable level. Fewer features not only improve the classifier performance but also provide faster computation and better understanding the underlying mechanism of the problem (Guyon and Elisseeff, 2003).

3.1. Feature extraction

Feature extraction is the process of transforming the raw data (in our problem it is the pixel gray values) into a set of reduced descriptive features. Massive amount of data in hyperspectral image cube can be described by features of a lower dimension by applying the feature extraction process. PCA and Auto-Associative Artificial Neural Network (ANN) are used for further reduction of the feature vector size. PCA maps high dimensional features onto a lower dimensional space by selecting the principal eigenvectors. Similarly, Autoassociator is equivalent to PCA if only one hidden layer is used as a bottleneck layer in the network topology and a linear activation function is used. It may outperform the PCA when an appropriate non-linear transformation is employed (Bourlard and Kamp, 1988). Let us assume the pixel gray value located at *x, y* of the *k*'th spectral band is denoted by $\boldsymbol{I_k(x,y)}$. We extract the following feature vectors.

Individual band energy features:

$$\boldsymbol{e_k} = \sum_x \sum_y \boldsymbol{I_k}(\boldsymbol{x}, \boldsymbol{y}) \qquad k = 1,2, \dots 33 \tag{1}$$

Absolute difference of consecutive spectral band energy features:

$$\boldsymbol{e_k} = \sum_x \sum_y |\boldsymbol{I_{k+1}}(\boldsymbol{x}, \boldsymbol{y}) - \boldsymbol{I_k}(\boldsymbol{x}, \boldsymbol{y})| \qquad k = 1,2, \dots 32 \tag{2}$$

Here, $I_k(x, y)$ and e_k correspond to pixel gray level intensity at image point (x,y) and energy value for the k th spectral band, respectively. The feature vectors described in Expressions 1 and 2 reduce the information in a given band to a single value. However, the frequency of a particular intensity value or the frequency of the difference of the intensity values may provide valuable information. This information can be extracted if the histogram of the intensity values or the difference of the intensity values for a given spectral band is used.

Figure 5 and Figure 6 present extracting processes of the quantized histogram matrix features. As it is shown in Figure 5, the histogram of the spectral band image is first computed with predefined number of bins. This limits the feature vector size and also promotes that a reasonable number of pixels fall in each bin. Then, the total number of pixels within the particular bin is used as the histogram feature. By using all spectral bands we can construct the quantized histogram matrix (QHM) as depicted in Figure 6. For simplicity we only demonstrate the extraction process for 12 bins. Different numbers of bins were also used and we will describe them in section 4 in detail.

QHM feature set is expected to contain the aflatoxin signature. This signature may be degraded if the overall mean intensities of the spectral bands are used instead. The QHM features are computed both for individual spectral bands and also for the absolute difference of consecutive spectral bands. Hence the QHM features can be expressed as

$$e_{k,n} = \sum_x \sum_y I_{k,n}(x,y) \qquad k = 1,2,\ldots 33 \;\; n = 1,2,\ldots B \tag{3}$$

Where k denotes index of spectral band, n denotes the bin index and B denotes number of bins that we want to employ. As a result, $I_{k,n}(x,y)$ is the pixel gray value of the kth spectral band or absolute difference of consecutive spectral bands of the nth bin.

Figure 5. a) A sample image (640 nm). b) Representative gray level histogram of the image in (a) to 12 bins. The color of the histogram bar at the bottom depicts the total number of pixels falling in each bin.

Figure 6. Quantized histogram matrix (QHM) is composed of histogram bars. a) Individual spectral band energies b) Absolute difference of consecutive spectral band energies. X axis denotes the spectral bands (or band pairs in the case of absolute difference) and Y axis denotes histogram bar for that band.

3.2. Feature selection

The main objective of the feature selection is to reduce the feature vector size without modifying the feature values. As the features are computed for each band separately in our problem, reducing the feature size removes the need for acquiring the corresponding image along the spectral axis. As a result, a more compact machine vision system can be established. Moreover, the dataset may contain redundant, irrelevant and/or noisy features. Removing these features is expected to yield higher and more robust classification rates. Feature selection can be divided into two main categories. First is the feature ranking. The second is the feature subset selection. Feature ranking is the process of sorting the candidate features according to their predictive significance. Although this approach is computationally efficient, determining the number of features is still an open problem. Selecting the top N features is intuitive but there is a possibility of retaining highly correlated features as in the hyperspectral imaging domain. In this study we used feature ranking scheme based on the Fisher discrimination power and employed the feature selection method to reveal the most discriminative features. Fisher discriminant was first proposed by Fisher, R.A. (1936) and is utilized in various studies. Fisher discrimination projects data from n-dimensional space to a one-dimensional space where between class scatter is maximum and within class scatter is minimum. It can be computed as;

$$F_{dp} = \frac{|\mu_1 - \mu_2|^2}{\sigma_1^2 + \sigma_2^2} \tag{4}$$

Here, F_{dp} is Fisher discrimination power, μ_i and σ_i denote the mean and standard deviation of the ith class respectively. Figure 7 depicts composite illustration of the boxplot (a) of the individual spectral bands with their Fisher discrimination power (b). The boxplot at the top shows the 50 percentile of the mean energy features of the contaminated (lighter color) and uncontaminated (darker color) chili peppers after z-score normalization over each spectral band. The horizontal bar beneath indicates the spectral bands value from 400 nm to 720 nm with 10 nm width. It can be observed that, uncontaminated chili pepper samples have relatively higher intensity levels than the contaminated ones. However, there are many samples that lie at the tails of the energy distribution (outliers) and the mean energy value distributions overlap significantly. Therefore, a threshold value that would separate the data into two distinct classes cannot be determined. The Fisher discrimination power for each spectral band is computed using Expression 4 and depicted in the bottom graph. Consistent with the boxplot above, the higher discrimination values are observed between 540 to 640 nm spectral bands. Similarly, Figure 8 illustrates integrated box plot of the absolute difference energies of consecutive spectral band features and Fisher discrimination power values. Most discriminative spectral bands lie between 520 to 570 nm.

Figure 7. a) Boxplot, b) Fisher discrimination power, of the individual spectral band energy features.

Figure 8. a) Boxplot, b) Fisher discrimination power, of the absolute difference of consecutive spectral band energy features.

For feature subset selection, we propose a novel feature subset selection method based on the MLP connection weights. By saying MLP we actually mean special case of one hidden-layer, feed-forward neural network trained by the well known back propagation algorithm (Rumelhart et al., 1986). Garson, (1991) stated that one can define feature saliency metric as:

$$\boldsymbol{\tau_i} = \sum_{\boldsymbol{j=1}}^{\boldsymbol{N}} \left| \boldsymbol{W_{ji} W_j} \right| \qquad\qquad i = 1,2,..M \tag{5}$$

Here, $\boldsymbol{\tau_i}$ denotes saliency metric of the ith feature. M *and* N are the number of input and hidden nodes, respectively. W_{ji} is the connection weight between the ith node of the input layer and jth node of the hidden layer. Similarly, W_j denotes the connection weight between jth node of the hidden layer to the output. In addition to this, Olden and Jackson, (2002) used Garson's algorithm and sensitivity analysis by applying randomization approach to show that MLP based variable selection can be applied and interpreted successively in the ecological domain. Each feature/variable is represented as an input node in the neural network topology. Let N be the number of hidden neurons in the hidden layer. As Figure 9 indicates ith feature's saliency metric can be computed as the sum of the absolute product of the connection weights from the *i*th input node through the hidden nodes to the output node.

Figure 9. MLP with input, hidden and output layer. W_{ji} is the connection weight between *i*th input node and *j*th hidden node. Similarly, W_j is the connection weight between *j*th hidden node and the output node.

The logic behind MLP based feature saliency metric is as follows. Connection weights are continuously updated in the training phase so that significant input nodes have strong connections in the network topology which means those input nodes have higher contribution to the output. Likewise, connection weights of the irrelevant features tend to vanish. Hence, MLP based feature saliency metric can be used as a dimensionality reduction technique by decaying the connection weights of the insignificant features. Moreover, the saliency can also be instrumental in ranking the features based on their discrimination power. This approach was taken in our previous study (Atas et al., 2011)

We propose a novel feature subset selection technique based on the MLP feature saliency metric. Forward selection and backward elimination were extensively used subset selection methods and regarded as robust to over fitting (Guyon and Elisseeff, 2003). Again, Guyon et al, (2002) proposed a state of the art support vector machine based recursive feature elimination method (RFE). In the RFE approach, the search starts with complete feature set. The features are ranked according to their predictive significance at every iteration and the least significant one is removed from the feature set. This procedure proceeds until some criterion is met. One can remove a single or last *N* features. Eliminating one feature per iteration is computationally costly, especially if you have large number of features. Thus, we modified the RFE method of Guyon et al, (2002) by replacing the central classifier SVM by MLP and we accelerated the process by removing last *N* features at each iteration where *N* is equal to the number of hidden neurons in the MLP network. Determining the optimal number of neurons in the hidden layer is still an open problem in the ANN domain. Yet there are some rules of thumb which are extensively used by the researchers (Rapid Miner, 2009, Berry and Linoff, 1997, Boger and Guterman, 1997, Blum, 1992). Specifically, the Rapid Miner team (2009) suggested number of neurons in the hidden layer to be:

$$N_{nodes} = \frac{(N_{features} + N_{classes})}{2} + 1 \qquad (6)$$

Here, N_{nodes} denotes the number of nodes in the hidden layer, $N_{features}$ is the number of features used as input nodes. In our trials, this approach gave satisfactory results so we used it. The procedure consists of two main stages: Backward elimination and subset verification. At the backward elimination stage, the candidate feature set is ranked based on the MLP saliency metric and the last N_{nodes} as in Expression 6 are eliminated. This process is repeated until only one feature remains. The number of steps, *M*, required for *P* original features is given by

$$M \cong log_2 P \qquad (7)$$

The candidate feature subset at every step is recorded in an array list data structure as shown in Figure 10. After the feature elimination process is completed, subset verification is initialized. At this stage, starting from the lowest feature subset (which typically consists of a single feature) generalization errors for each feature subset are computed. If there are *L* ranked features at a given subset, the generalization error for i) only one, ii) first two, iii) first three, etc. features are computed using leave-one-out cross validation strategy. The computational cost associated with this step increases exponentially with increasing the number of ranked features *L*. Therefore, we only computed generalization errors for the first five levels from the bottom of the triangle in Figure 10. We chose the feature subset which yielded the minimum generalization error. In the case of similar generalization errors we preferred the smaller size of features amongst the candidate feature subsets. We used non-random V shape (triangular) weight initialization scheme for the connection weights between input and hidden layer. That way, reproducible results could be obtained during the feature selection process. Bias values were set to zero at start up.

Figure 10. Proposed HBBE method. *L* and *M* designate the number of features and the number of steps, respectively.

3.3. Classifier selection

We decided to utilize both a simple classifier and a complex classifier for our problem. For linearly separable problems, Linear Discriminant Analysis (LDA) provides good classification performance. Moreover due to its simplicity LDA is less susceptible to over fitting the training data which provides robustness. Thus, LDA was selected as the first classifier. As the second classifier, we preferred to use a feed forward back propagated one hidden layered artificial neural network also known as the MLP. MLP is extensively used in various studies and is regarded as the universal approximator of any continuousfunction (Hornik et al, 1989). Elmasry et al., (2009), Bochereau et al., (1992) and Jayas et al. (2000) reported that, ANN is very efficient for identification and classification of agricultural products which contain non-linearity. In particular, Kim et al. (2000) pointed out that, MLP is superior to linear classifiers in terms of prediction accuracy for the classification of kiwi fruit berries. Again, Park and Chen (1996) utilized ANN with a spectral imaging technique and successively achieved 93.3% generalization performance for classifying wholesome chicken carcasses from unwholesome ones. Thus, we selected MLP as the second classifier in this study. In addition to these, SVM with linear kernel classifier was also used within the SVM-RFE method.

4. EXPERIMENTAL RESULTS

Hyperspectral image series with 33 spectral bands at two different illumination modes (halogen and UV) of 53 chili pepper samples were acquired. Images of three different locations of each chili pepper sample yielded a total of 10494 images of 1280x960 resolution. It should be noted that, during the evaluation stage, images of the same chili pepper samples were isolated from the training data so that unbiased accuracy results can be achieved. By using Equation 1 and Equation 2, feature vectors with size of 33 individual spectral band energy features and size of 32 absolute differences of consecutive spectral band energy features were extracted. The other two types of feature sets were extracted according to Equation 3. They are, quantized individual spectral band energy features and quantized absolute difference of consecutive spectral band energy features. We tried 6, 12, 24 bins feature set and achieved best discrimination power with 12 bins. The total number of features in the quantized individual spectral band was 33 (spectral bands) x 12 (quantization bins) = 396. Similarly for the quantized absolute difference of consecutive spectral band, originally we had 32 (difference spectral band pairs) x 12 (quantization bins) which resulted in 384 features. As it is seen in Figure 6, there exists high number of zero value features in the feature set. MLP typically discards those features in the first step.

All the data were normalized according to Z-Score normalization yielding the distribution of the data with zero mean and unit variance. The learning rate, momentum coefficient and the number of epochs were adjusted adaptively with the rate of convergence. The learning rate and the momentum value were initialized as best practices to 0.1 (Cravener and Roush, 1999, Rajanayaka et al., 2003), and decayed during the learning phase. Decaying procedure is summarized in Figure 11. By this way it is expected to prevent the classifier from over-fitting and under-fitting. As Hornik et al. (1989) and Malek et al. (2000) pointed out, MLP with a single hidden layer is adequate as a universal approximator. We also employed a single hidden layered network topology in our study. The number of hidden nodes in the hidden layer was determined via the Expression 6.

Figure 11. Schematic diagram of the decaying procedure of the learning rate and momentum values.

K-fold cross validation technique was utilized for the evaluation of generalization performance. In the machine learning community, K is commonly selected as 10 or 5 (Breiman and Spector, 1992, Wassenaar et al., 2003). Therefore in this study we used K as 5. We partitioned our data set randomly into five disjoint folds. Four folds were used for training and validation purposes and the remaining fold was utilized as the unseen test data for our predictive model. Since our data is limited, we would like to exploit all the data at the training and validation set. Thus, we preferred to employ leave one out cross validation (LOO-CV) technique for training and validation set. The final decision on aflatoxin presence is made using majority voting on the three images of the same chili pepper. This process was repeated for each fold and average accuracy rate was computed from the five folds test results.

In order to assess the effectiveness of our proposed method we compared its classification accuracy rates with those of the original features and reduced features by applying PCA, SVM-RFE and

Fisher methods. To achieve a fair comparison with HBBE and SVM-RFE algorithms, feature selection process was also employed on the PCA and Fisher methods. Table 2 shows overall accuracy rates of several feature sets with various feature selection methods under the halogen and UV illuminations. Average number of features used for each methods are given below the accuracy rates in parentheses. As Table 2 indicates, in most cases, HBBE method outperforms other. Even PCA gives higher accuracy in two cases (Halogen-individual band and UV-absolute difference), HBBE is still preferable since PCA uses all the spectral bands which is not a desired property for constructing a simple machine vision system.

Table 2. Generalization performance of the extracted features MLP versus LDA classifiers under halogen and UV excitations.

As it can be seen from Table 2, taking the absolute difference of consecutive spectral bands generally improves the classification performance for both halogen and UV excitations.. Similarly quantization process increases the accuracy rate in almost all the feature sets.

Table 3 compares the best results obtained by our proposed methods to wavelet LDB method of Kalkan et al. (2011). Best results for Dataset-1 and Dataset-2 are shown in bold. As it is seen in the table, our proposed method outperform wavelet LDB method. This comparison was made for two datasets. The Dataset-1 which consists of 53 new chili pepper samples using electronically tunable filter, is the spectral data acquired for this research, the Dataset-2 comprises 40 chili pepper samples imaged using optical filters with full width half maximum (FWHM) 400 to 600 nm as described in

(Kalkan et al., 2011) study. We should emphasize that the bands 520-720 nm with 10 nm width were not available in the Dataset-2.

Table 3. Benchmark of the proposed method against wavelet LDB method for Dataset-1 and Dataset-2

In the case of the Dataset-2, the quantized individual band energy features yield better accuracy rates than the quantized absolute difference energy features. This may be due to the fact that we fixed the camera gain parameter to 850 electron/CCD and manually changed the exposure time that blocked the running of histogram equalization process at the background while acquiring the images of the Dataset-1. On the other hand, Dataset-2 was acquired under the automatic gain parameters enabling automatic histogram equalization which may modify the original spectral signal. Although histogram equalization aims to enhance the image quality and yields visually appealing images, it will also modify the spectral signature. This may degrade the features based on absolute difference of consecutive spectral bands more than individual band energy features. Therefore individual spectral bands may contain more informative pattern than the absolute difference of consecutive spectral bands. As a result, wavelet features and quantized individual spectral band energy features produced relatively better results than the absolute difference features under the UV excitation. Table 2 and Table 3 reveal that aflatoxin detection in chili pepper problem is not a linearly separable problem because almost in all cases MLP outperforms LDA in terms of classification accuracy.

As it seen in Table 3, the highest classification accuracy on the Dataset-1 was obtained with absolute difference of QHM features selected by the HBBE feature subset selection using MLP classifier as 83.26% under halogen illumination. Similarly, the highest classification accuracy on the Dataset-2 was obtained with individual band of QHM features selected by the HBBE feature subset selection using MLP classifier as 87.5% under UV illumination.

Figure 12 illustrates the features selected by 5 fold cross validation of QHM features based on HBBE feature selection under the halogen illumination for the Dataset-1. The features selected at each fold are added to the corresponding bin. As the QHM features require two consecutive bands to be used, each feature contributes to the tally in two bins. To determine which spectral band images should be acquired in the machine vision system. In Figure 12, the most discriminative spectral bands and features can be seen. The most informative bands are 540, 550, 560, 590, 640 and 650 nm if voting threshold value 4 is selected .

Figure 12. Dataset-1 vote map for visualizing the most frequently selected spectral bands with the associated bin numbers.

In Figure 12, the frequency of each feature is indicated on the corresponding feature cell. The frequency count of a particular spectral band is the total of the frequency counts of all bins in that spectral band. Dark color indicates high frequencies whereas light color means low frequencies. Completely white cells are the features with insignificant contribution to classification. Proposed feature selection scheme eliminates those features and reduces the feature dimension. We can extract series of most discriminative spectral bands by applying different threshold values. Table 4 depicts, most discriminative spectral bands based on different threshold values associated with LOO-CV accuracy rates.

Table 4. Most discriminative spectral bands based on different threshold values associated with LOO-CV accuracy rates for the Dataset-1.

Table 4 indicates that there is a tradeoff between the accuracy rate and number of features selected which will determine the design of the machine vision system. Higher classification performance may require higher numbers of spectral filters which will increase the complexity of the overall machine vision system. On the other hand, establishing a relatively simpler machine vision system can be realized at the expense of lower generalization performance.

We repeated the same scenarios for the Dataset-2 as well. Figure 13 and Table 5 demonstrate the most frequently selected spectral bands and threshold features respectively.

Figure 13. Dataset-2 vote map for visualizing the most frequently selected spectral bands with the associated bin numbers.

Table 5. Most discriminative spectral bands based on different threshold values associated with LOO-CV accuracy rates for the Dataset-2.

It is seen from Table 5, for the Dataset-2, simpler machine vision system with single spectral band of 420 nm is sufficient to achieve 85% classification accuracy. On the other hand, if 400 nm is also used in the system, 90% classification accuracy would be possible.

5. CONCLUSION

In this study, detection of aflatoxin contaminated chili pepper was investigated. Both UV and Halogen illuminations were used. Hyperspectral image series of 53 the Dataset-1 were acquired. Absolute difference of consecutive spectral band energy features was proposed. Another set of quantized histogram matrix features (QHM) were extracted from individual spectral bands and absolute difference of consecutive spectral bands by applying the quantization process. The most discriminative features were constructed with 12 bins quantization. In addition to these, a novel feature selection method was also proposed based on saliency metric of MLP connection weights. This approach was compared to PCA and Fisher methods. 83.26% accuracy rate was achieved for the Dataset-1 under the halogen illumination with proposed QHM features and HBBE feature selection method. Utilizing halogen is superior to UV. The most frequently selected spectral bands for the Dataset-1 were 540, 550, 560, 590, 640 and 650 nm. We used LDA as a simple linear classifier and MLP as a complex non-linear classifier. Experimental results reveal that MLP outperforms LDA in terms of classification accuracy rate. Robustness of our proposed methods was verified by the Dataset-2 under the UV excitation and we achieved 87.50% classification accuracy. 400 and 420 nm spectral bands were selected as the most discriminative spectral bands for the Dataset-2. With the reduced spectral bands, it will be possible to construct a simple machine vision system for aflatoxin detection in chili pepper.

6. ACKNOWLEDGEMENTS

This research was made possible by a grant from the National Scientific Research Council of Turkey (TUBITAK) project 106E057.

7. REFERENCES

Ataş, M., Yardimci, Y., Temizel, A., 2011. Aflatoxin Contaminated Chili Pepper Detection by Hyperspectral Imaging and Machine Learning. Sensing for Agriculture and Food Quality and Safety III Proc. SPIE.

Berry, M.J.A., Linoff, G. 1997. Data Mining Techniques, NY: John Wiley & Sons.

Blum, A., 1992, Neural Networks in C++, NY: Wiley.

Bochereau, L., Bourgine, P., Palagos, B., 1992. A method for prediction by combining data analysis and neural networks: application to prediction of apple quality using near infra-red spectra. Journal of Agricultural Engineering Research 51 (2), 207–216.

Boger, Z., and Guterman, H., 1997, "Knowledge extraction from artificial neural network models," IEEE Systems, Man, and Cybernetics Conference, Orlando, FL, USA

Bourlard, H., Kamp, Y., 1988. Auto-Association by Multilayer Perceptrons and Singular Value Decomposition, Bio. Cybernetics, 59, 291-294.

Breiman, L., and Spector, P. 1992. Submodel selection and evaluation in regression: The X-random case, International Statistical Review, 60, 291-319.

Chen, J.M., Zhang, X.H., Yang, M.H, Jin, Y., 2005. Recent advances in the determination methods of aflatoxins, China Journal of Chinese Materia Medica, 24.

Cravener, T.L. and W.B. Roush, 1999. Improving Neural Network Prediction of Amino.Acid Levels in Feed Ingredients. Poultry Science 78:983-991.

Doster, M.A., T.J. Michailides and D.P. Morgan, 1996. Aspergillus Species and Mycotoxins in Figs from California Orchards. Plant Disease, 80: 484-489.

EC (2006). European Commission Regulation (EC) No 1881/2006 of 19 December 2006: Setting maximum levels for certain contaminants in foodstuffs, Official Journal of the European Union.

ElMasry, G., Wangb N., Vigneault, C., Qiao J., ElSayed A., 2007. Early detection of apple bruises on different background colors using hyperspectral Imaging, LWT, 41, 337-345.

ElMasry, G., Wangb N., Vigneault, C., 2009. Detecting Chilling Injury In Red Delicious Apple Using Hyperspectral Imaging And Neural Networks, Postharvest Biology and Technology, 52(1), 1-8.

Fersaie, A., McClure, W.F. and Monroe, R.J., 1978. Development of Indices for Sorting Iranian Pistachio Nuts According to Fluorescence, Journal of Food Science 43(3): 1550-1552.

Fisher, R.A., 1936. The Use of Multiple Measurements in Taxonomic Problems, Annals of Eugenics, 7, 179-188.

Garson, G.D., 1991. Interpreting Neural Network Connection Weights., Artificial Intelligence Expert, 6(4), 47–51.

Guyon, I., Elisseeff A., 2003. An Introduction to Variable and Feature Selection, Journal of Machine Learning Research, 3, 1157-1182.

Guyon, I., Weston, J., Barnhill, S., Vapnik, V., 2002. Gene selection for cancer classification using support vector machines. Machine Learning, 46, 389–422.

Herrman, T., 2002.Mycotoxins in Feed Grains and Ingredients, Feed Manufacturing, Kansas State University.MF-2061.

Hirano, S., Okawara, N., Narazaki, S., 1998. Near Infra Red Detection of Internally Moldy Nuts, Bioscience, Biotechnology, and Biochemistry, 62, 102-107.

Hornik, K., Stinchcombe, M., White, H., 1989. Multilayer feedforward networks are universal approximators. Neural Networks 2, 359–366.

IARC. 2002. Aflatoxins. In Traditional Herbal Medicines, Some Mycotoxins, Naphthalene and Styrene., IARC Monographs on the Evaluation of Carcinogenic Risks to Humans, 82, 171-366.

Jayas, D.S., Paliwal, J., Visen, N.S., 2000. Multi-layer neural networks for image analysis of agricultural products. Journal of Agricultural Engineering Research 77 (2), 119–128.

Kalkan, H., Beriat, P., Yardimci, Y., Pearson, T.C., 2011. Detection of contaminated hazelnuts and ground red chili pepper flakes by multispectral imaging., Computers and Electronics in Agriculture, 77, 28-34.

Kim, J., Mowat, A., Poole, P., Kasabov, N., 2000. Linear and non-linear pattern recognition models for classification of fruit from visible–near infrared spectra. Chemometrics and Intelligent Laboratory Systems 51, 201–216.

Malek, J.E., Alımı, A.M., Tourki, R., 2000. Effect of the Feature Vector Size on the Generalization Error: The Case of MLPNN and RBFNN Classifiers, ICPR, 2, 2630.

Olden, J.D., Jackson, D.A., 2002. Illuminating the Black Box: a Randomization Approach for Understanding Variable Contributions in Artificial Neural Networks., Ecological Modeling, 154, 135–150.

Park, B., Chen, Y.R., 1996. Multispectral image analysis using neural network algorithm. ASAE Paper No. 96-3034.

Pearson, T., Wicklow, D., Maghirang, E., Xie, F. and Dowell, F., 2001. Detecting Aflatoxin in Single Corn Kernels by Using Transmittance and Reflectance Spectroscopy., Transactions of the ASAE, 44(5), 1247-1254.

Rajanayaka, C., Kulasiri, D., and Samarasinghe, S., 2003. A comparative study of parameter estimation in hydrology modelling: Artificial neural networks and curve fitting approaches. Proceeding of International conference on Modelling and Simulation.

Rapid Miner Tool, 2009. Neural Net Learner (Rapid Miner Class Documentation) [Online]. Available at : http://rapid-i.com/api/rapidminer-4.4/com/rapidminer/operator/learner/functions/neuralnet/NeuralNetLearner.html [Accessed: 15 August 2011].

Rumelhart, D.E., Hinton, G.E., Williams, R.J., 1986. Learning representations by back-propagation errors. Nature, 323, 533–536.

Sakthivel, S., Lakshmipathi, Dr.R., 2010. Weighted Attribute Fusion Model for Face Recognition, International Journal of Computer Science and Information Security, 8(3), 122-128.

Shotwell, O.L., Goulden, M.L., Hesseltine, C.W., 1972. Aflatoxin contamination: Association with foreign material and characteristic fluorescence in damaged corn kernels. Cereal Chern. 49:458.

Singh C.B., Jayas D.S., Paliwal J., White N.D.G., 2010. Identification of Insect-Damaged Wheat Kernels Using Short-Wave Near-Infrared Hyperspectral and Digitial Colour Imaging. Computers and Electronics in Agriculture Research, 73, 118-125.

Tyson, T.W., Clark, R.L., 1974. An Investigation of the Fluorescent Properties of Aflatoxin Infected Pecans, Transactions of the ASAE, 17(5), 942-944 .

Wagacha, J.M., Muthomi, J.W., 2008. Mycotoxin problem in Africa: Current status, implications to food safety and health and possible management strategies, Int. Journal of Food Microbiology., 124: 1-12.

Yao, H., Hruska, Z., Brown, R.L., Cleveland, T.E., 2006. Hyperspectral Bright Greenish-Yellow Fluorescence (BGYF) Imaging of Aflatoxin Contaminated Corn Kernels, Proc. SPIE, Optics for Natural Resources, Agriculture, and Foods, 6381, 63810B.

Yao, H., Hruska, Z., Kincaid, R., Ononye, A., Brown, R.L., Bhatnagar, D., Cleveland, T.E., 2011. Development of Narrow-band Fluorescence Index for the Detection of Aflatoxin Contaminated Corn, Proc. SPIE, Sensing for Agriculture and Food Quality and Safety III , 8027, 80270D.

Yang, S., Chen, M., Pomerleau, D., Sukthankar, R., 2010. Food recognition using statistics of pairwise local features. CVPR 2010: 2249-2256.

Zeringue, H.J., Shih, B.Y., 1998. Extraction and Separation of the BGYF Material from Aflatoxigenic Aspergillus spp. Infected Cotton Lint by HPLC-UV/FL, Journal of Agricultural and Food Chemistry, 46(3), 1071-1075.

Wassenaar, H. J., Chen, W., Cheng, J. and Sudjianto, A., 2003 Enhancing Discrete Choice Demand Modeling For Decision-Based Design. ASME 2003 Design Engineering Technical Conferences and Computers and Information in Engineering Conference, Chicago, Illinois USA. DETC’03.

TABLES

Illumination	Exposure time (s)	Normalization coefficient
Halogen (400-490) nm	4.5	1
Halogen (500-590) nm	2.4	1.875
Halogen (600-720) nm	0.5	9
UV (400-690) nm	9.6	1
UV (700-720) nm	3.1	3.09

Table 1: Exposure normalization coefficients of the most informative regions of the spectral bands.

Feature Extraction Method	Org. Feature size	MLP classification accuracy rates				SVM	LDA classification accuracy rates			
		Original	PCA	Fisher	HBBE	RFE	Original	PCA	Fisher	HBBE

Halogen	Individual Band Energy Features	33	62.34	**70.76 (11.4)**	67.94 (4.4)	68.16 (6.8)	56.54 (7.8)	37.64	66.73 (17.4)	65.16 (1.0)	34.00 (5.4)
	Absolute Difference Energy Features	32	62.52	69.36 (18.0)	71.29 (12.0)	**71.62 (5.4)**	71.45 (10.2)	50,70	63.03 (13.4)	64.76 (1.2)	43.64 (3.2)
	Quantized Individual Band Energy Features (12 bins)	396	61.98	67.43 (6.2)	67.92 (1.8)	**81.26 (11.0)**	76.00 (17.0)	48.88	65.46 (11.4)	70.66 (6.2)	60.70 (8.2)
	Quantized Absolute Difference Energy Features (12 bins)	384	60.34	64.70 (11.6)	71.21 (4.8)	**83.26 (5.8)**	71.81 (17.2)	50.88	67.85 (13.2)	72.44 (5.4)	61.98 (6.4)
UV	Individual Band Energy Features	33	63.80	63.11 (6.4)	63.83 (1.8)	**69.80 (3.0)**	47.45 (5.8)	33.84	69.18 (9.4)	65.17 (1.2)	35.82 (5.4)
	Absolute Difference Energy Features	32	62.52	**71.68 (11.6)**	71.20 (10.0)	65.98 (6.6)	60.00 (13.4)	48.90	61.44 (2.6)	62.78 (2.8)	49.44 (6.8)
	Quantized Individual Band Energy Features (12 bins)	396	58.34	61.30 (6.6)	61.91 (6.8)	**62.14 (11.8)**	48.54 (12.2)	48.88	60.46 (12.4)	61.56 (8.0)	50.90 (7.8)
	Quantized Absolute Difference Energy Features (12 bins)	384	58.34	62.27 (14.4)	**72.63 (13.4)**	67.98 (10.6)	54.90 (15.8)	48.90	61.23 (7.2)	66.72 (1.2)	52.90 (5.4)

Table 2. Generalization performance of the extracted features with different feature selection methods versus different classifiers under halogen and UV excitations.

Dataset	Illumination Source	Feature Extraction Type	Feature Selection	Classifier	Accuracy Rate
Dataset-1	Halogen	Quantized Absolute Difference Energy (12 bins)	HBBE	MLP	**83.26%**
			HBBE	LDA	61.98%
		Wavelet Features	LDB	MLP	63.64%
			LDB	LDA	62.44%
	UV	Quantized Absolute Difference Energy (12 bins)	HBBE	MLP	67.98%
			HBBE	LDA	52.90%
		Wavelet Features	LDB	MLP	61.82%
			LDB	LDA	57.10%
Dataset-2	UV	Quantized Individual Band Energy (25 bins)	HBBE	MLP	**87.50%**
			HBBE	LDA	67.50%
			LDB	MLP	77.50%

Wavelet Features	LDB[a]	LDA	74.65%

Table 3. Benchmark of the proposed method against wavelet LDB method for Dataset-1 and Dataset-2

	Dataset-1		
Threshold	Selected Bands (nm)	Feature size	LOO-CV Accuracy Rate
1	410-440, 510-560, 580-600, 620-690, 710,720	20	85%
2	430,440,520,540,550,560,580,590,630-670	15	81%
3	540,550,560,580,590,640,650,660	12	78%
4	540,550,560,590,640,650	9	68%
5	540,550,560	4	62%

Table 4. Most discriminative spectral bands based on different threshold values associated with LOO-CV accuracy rates for the Dataset-1.

	Dataset-2		
Threshold	Selected Bands (nm)	Feature size	LOO-CV Accuracy Rate
1	400,410,420,430,440,480,500,600	19	85%
2	400,410,420,430,440,600	17	85%
4	400,420,440	13	90%
6	400, 420	10	90%

[a] The results differ from those of Kalkan et al., (2011) as they partitioned the data set into 4 disjoint folds in their experiments, whereas we employed 5-fold cross validation. Even if the number of folds were the same, there might be slight differences on the accuracy rates due to chili pepper samples falling into different folds for different trials.

8	420	6	85%

Table 5. Most discriminative spectral bands based on different threshold values associated with LOO-CV accuracy rates for the Dataset-2.

List of Figure Captions

Figure 1. General overview of the hyperspectral imaging system.

Figure 2. Flowchart and interrelated components of the proposed system.

Figure 3. Histogram based Aflatoxin aflatoxin variations of chili pepper samples.

Figure 4. Sample images from the hyperspectral image series of uncontaminated and contaminated peppers for halogen and UV illuminations.

Figure 5. a) A sample image (640 nm). b) Representative gray level histogram of the image in (a) to 12 bins. The color of the histogram bar at the bottom depicts the total number of pixels falling in each bin.

Figure 6. Quantized histogram matrix (QHM) is composed of histogram bars. a) Individual spectral band energies b) Absolute difference of consecutive spectral band energies. X axis denotes the spectral bands (or band pairs in the case of absolute difference) and Y axis denotes histogram bar for that band.

Figure 7. a) Boxplot, b) Fisher discrimination power, of the individual spectral band energy features.

Figure 8. a) Boxplot, b) Fisher discrimination power, of the absolute difference of consecutive spectral band energy features.

Figure 9. MLP with input, hidden and output layer. W_{ji} is the connection weight between i'th input node and j'th hidden node. Similarly, W_j is the connection weight between j'th hidden node and the output node.

Figure 10. Proposed HBBE method. L and M designate the number of features and the number of steps, respectively.

Figure 11. Schematic diagram of the decaying procedure of the learning rate and momentum values.

Figure 12. Dataset-1 vote map for visualizing the most frequently selected spectral bands with the associated bin numbers.

Figure 13. Dataset-2 vote map for visualizing the most frequently selected spectral bands with the associated bin numbers.

FIGURES

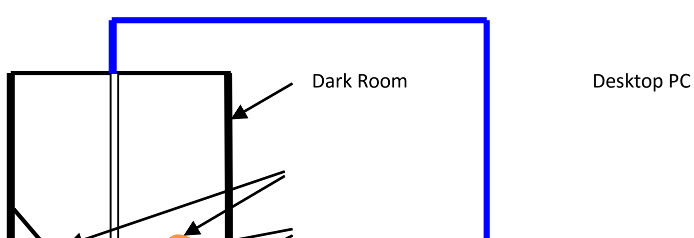

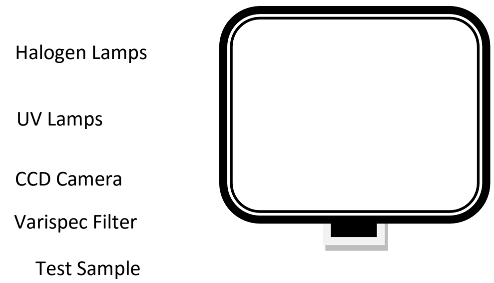

Figure 1

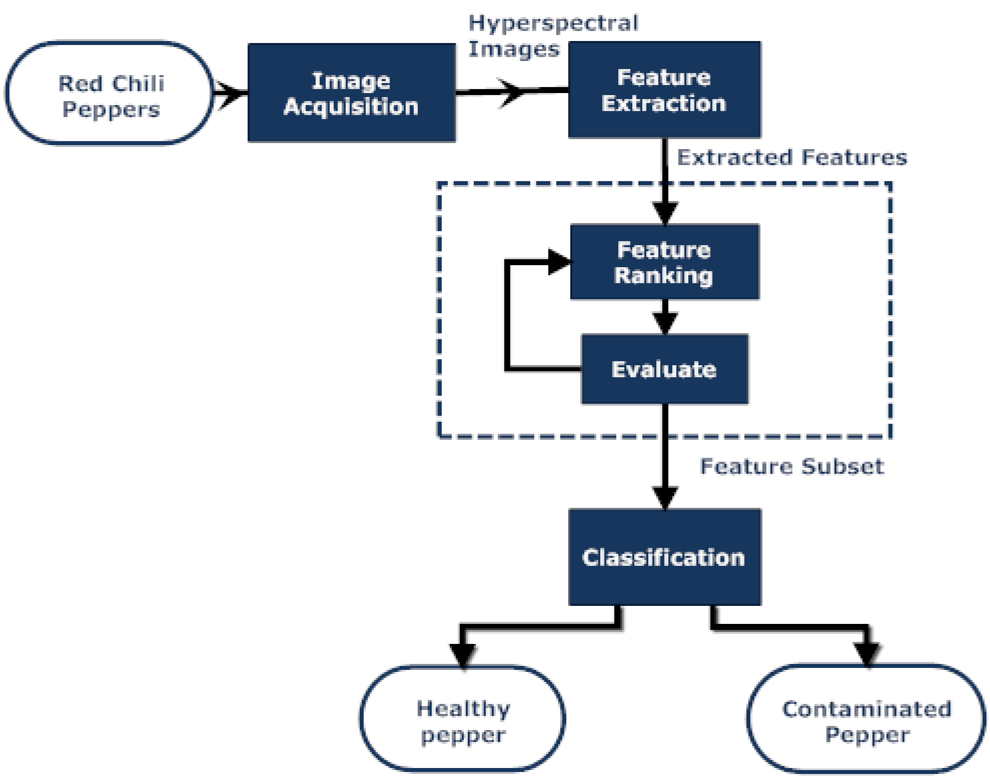

Figure 2

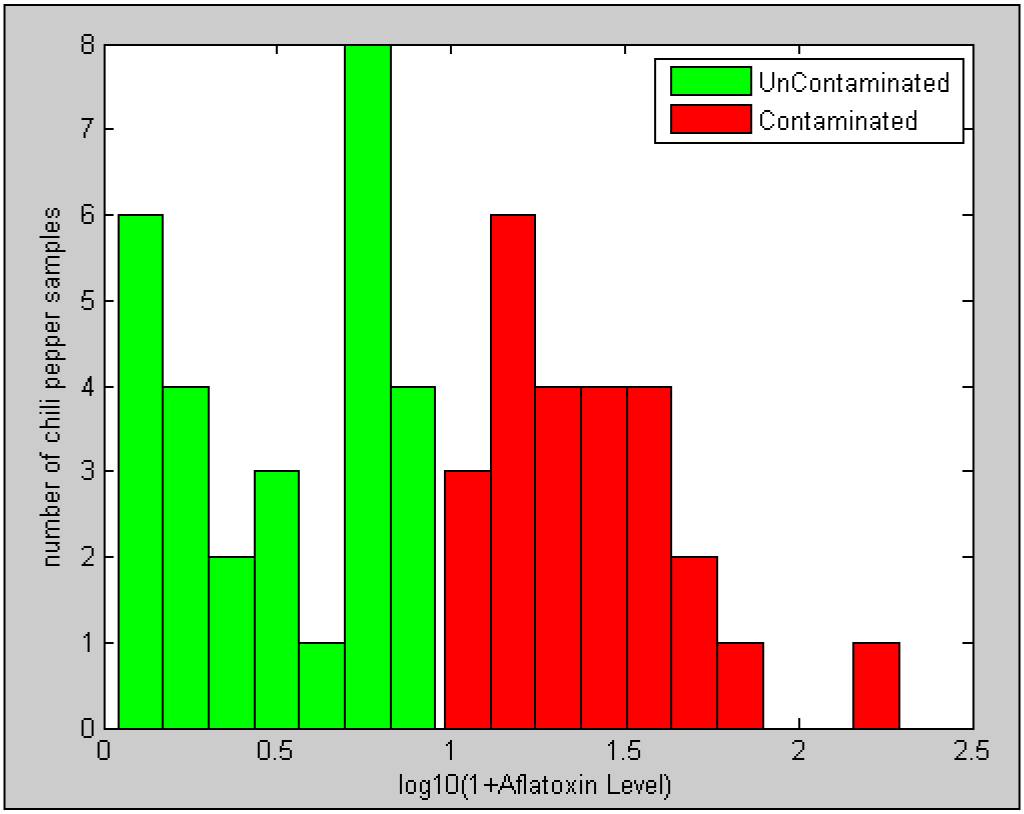

Figure 3

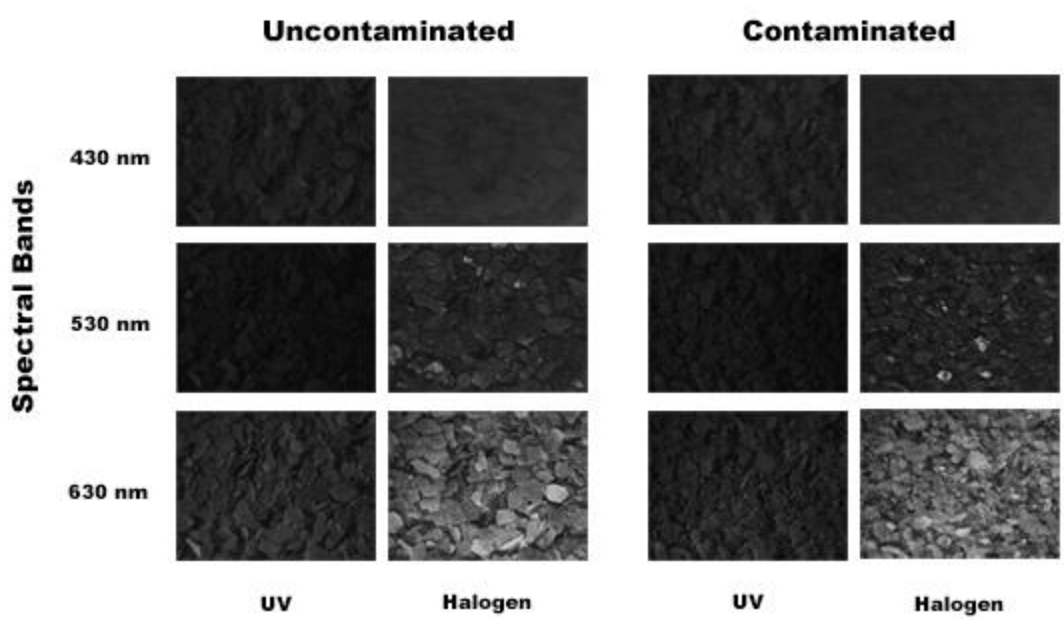

Figure 4

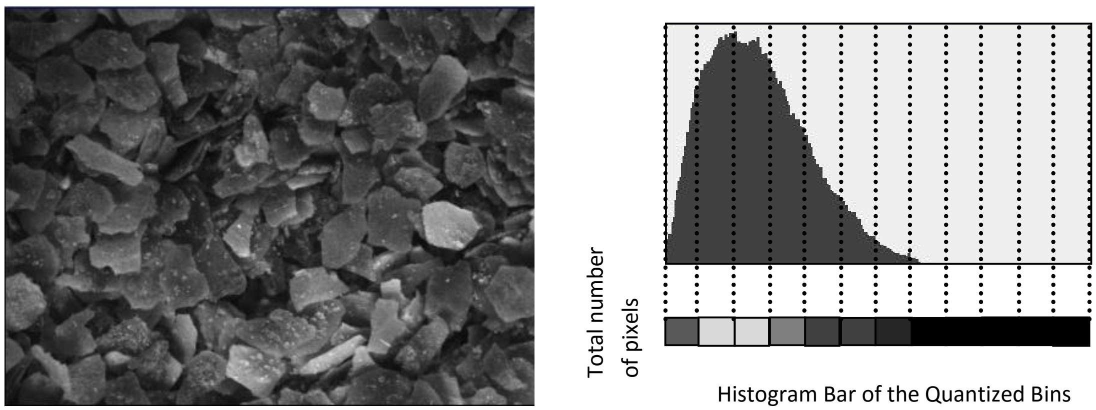

a) b)

Figure 5

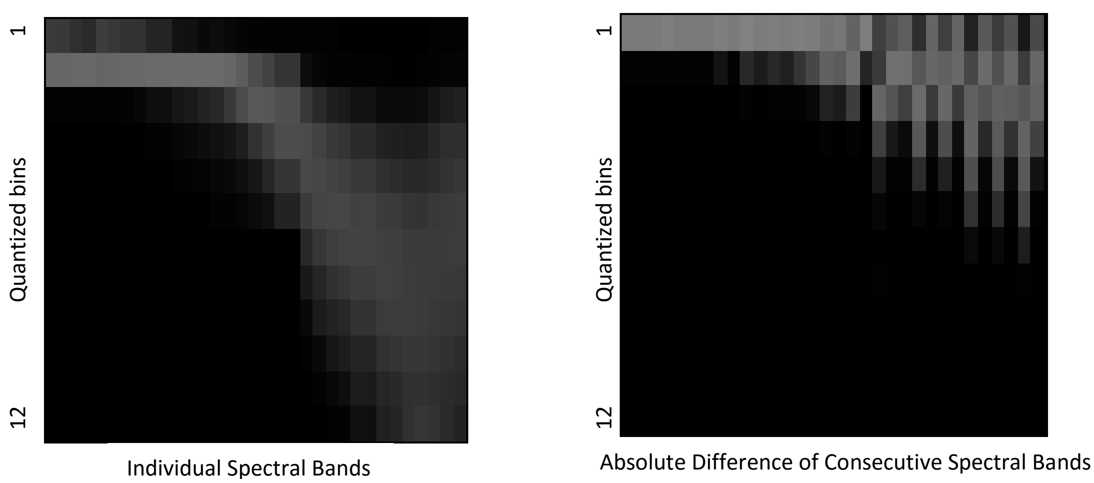

a) b)

Figure 6

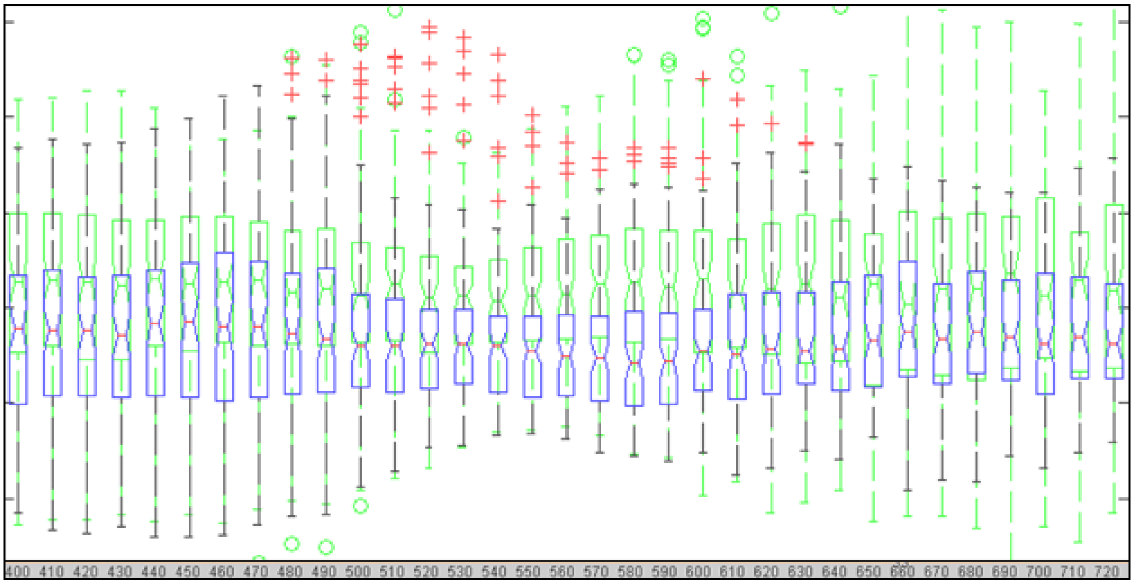
400 410 420 430 440 450 460 470 480 490 500 510 520 530 540 550 560 570 580 590 600 610 620 630 640 650 660 670 680 690 700 710 720

a)

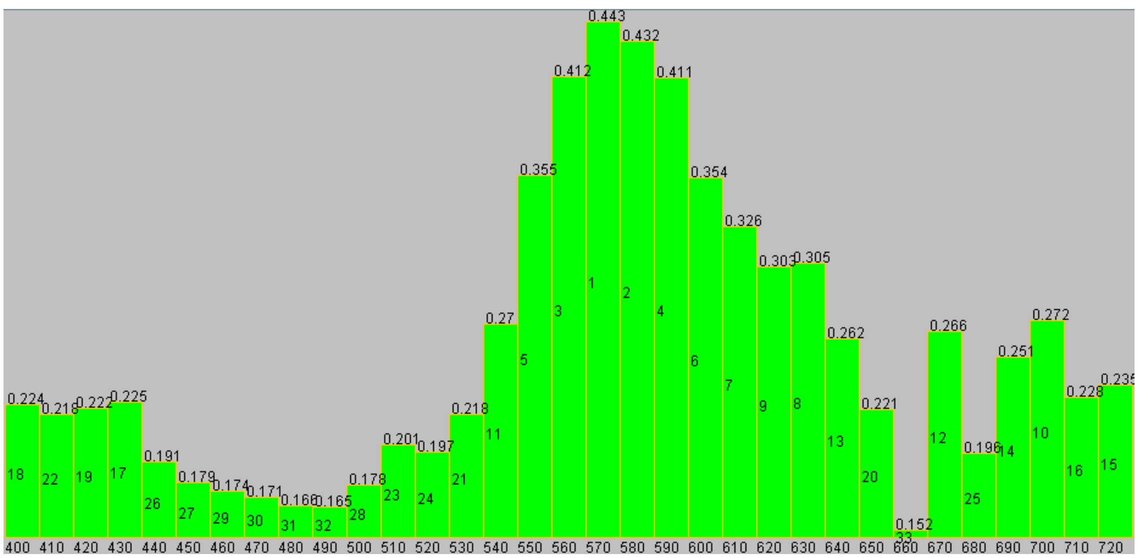
0.224
18
0.218
22
0.222
19
0.225
17
0.191
26
0.179
27
0.174
29
0.171
30
0.166
31
0.165
32
0.178
28
0.201
23
0.197
24
0.218
21
0.27
11
0.355
5
0.412
3
0.443
1
0.432
2
0.411
4
0.354
6
0.326
7
0.303
9
0.305
8
0.262
13
0.221
20
0.152
33
0.266
12
0.196
25
0.251
14
0.272
10
0.228
16
15
400 410 420 430 440 450 460 470 480 490 500 510 520 530 540 550 560 570 580 590 600 610 620 630 640 650 660 670 680 690 700 710 720

b)

Figure 7

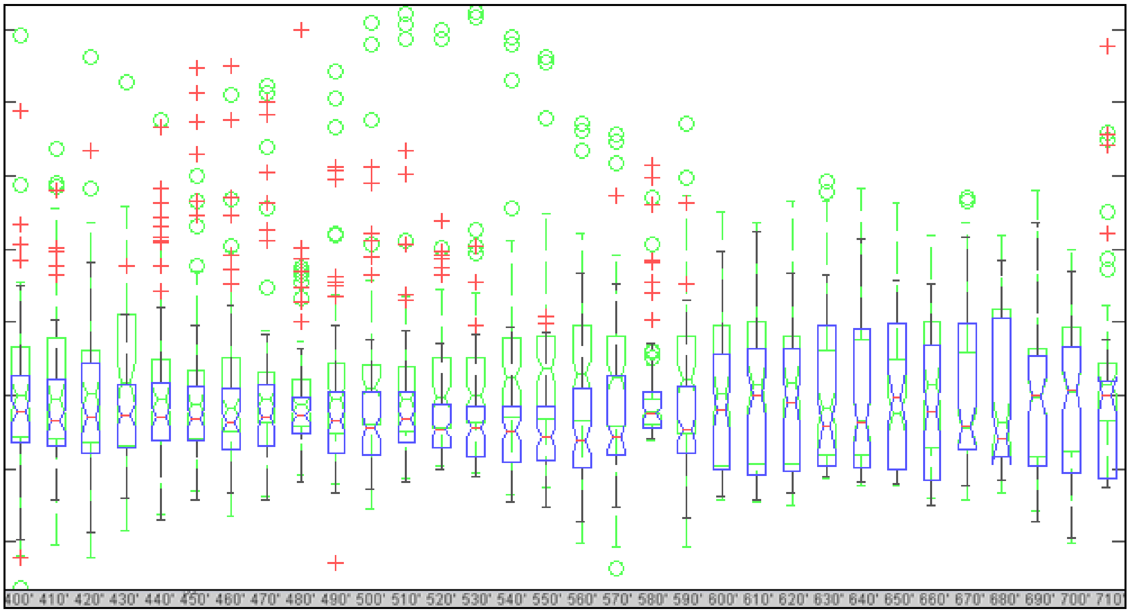
400' 410' 420' 430' 440' 450' 460' 470' 480' 490' 500' 510' 520' 530' 540' 550' 560' 570' 580' 590' 600' 610' 620' 630' 640' 650' 660' 670' 680' 690' 700' 710'

a)

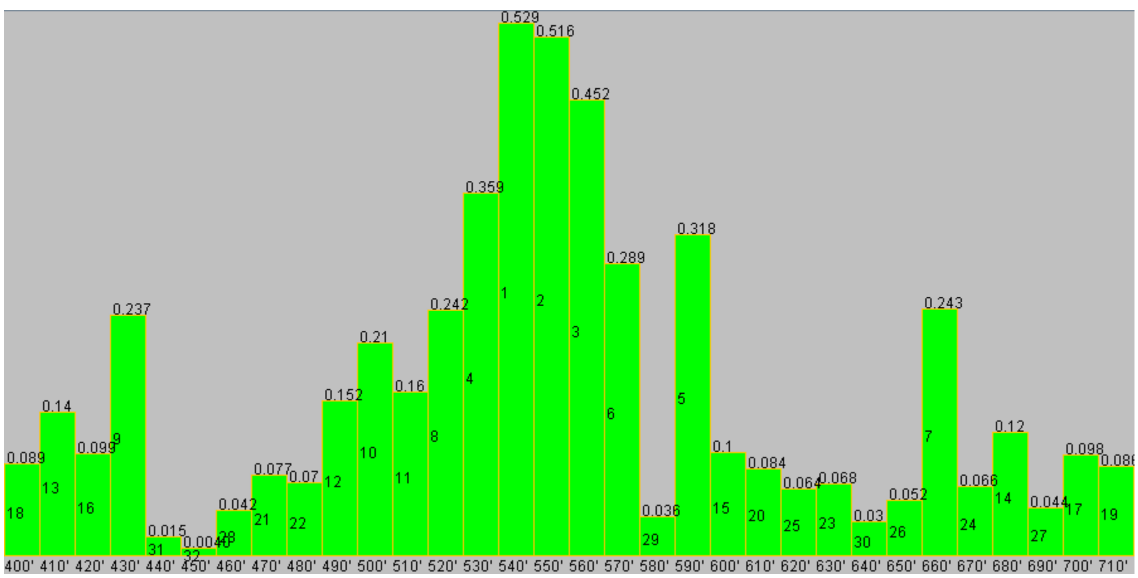
0.089
18
0.14
13
0.099
16
0.237
9
0.015
31
0.004
32
0.042
28
0.077
21
0.07
22
0.152
12
0.21
10
0.16
11
0.242
8
0.359
4
0.529
1
0.516
2
0.452
3
0.289
6
0.036
29
0.318
5
0.1
15
0.084
20
0.064
25
0.068
23
0.03
30
0.052
26
0.243
7
0.066
24
0.12
14
0.044
27
0.098
17
19
400' 410' 420' 430' 440' 450' 460' 470' 480' 490' 500' 510' 520' 530' 540' 550' 560' 570' 580' 590' 600' 610' 620' 630' 640' 650' 660' 670' 680' 690' 700' 710'

b)

Figure 8

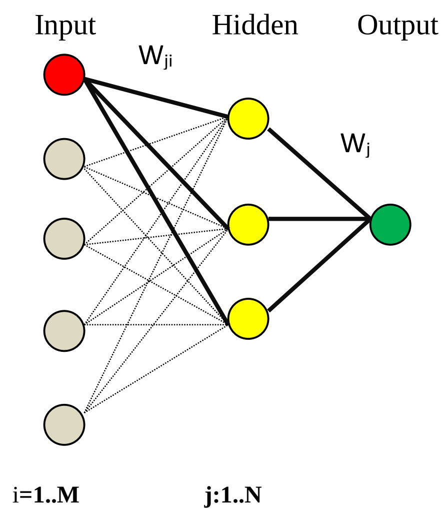

Figure 9

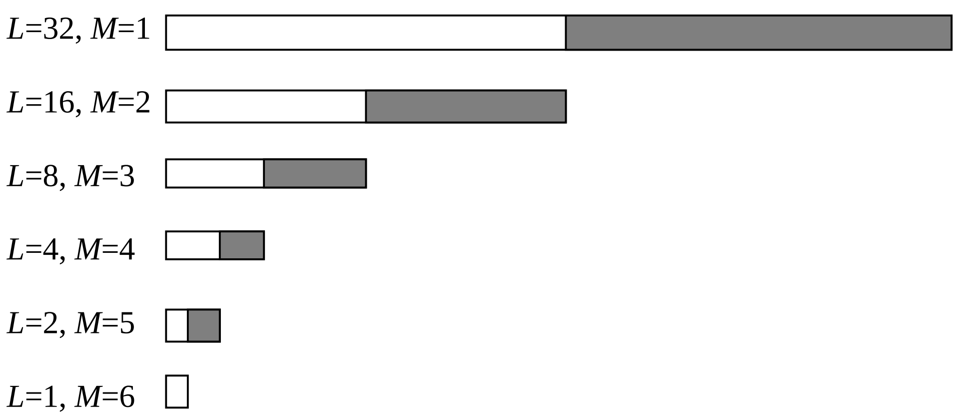

Figure 10

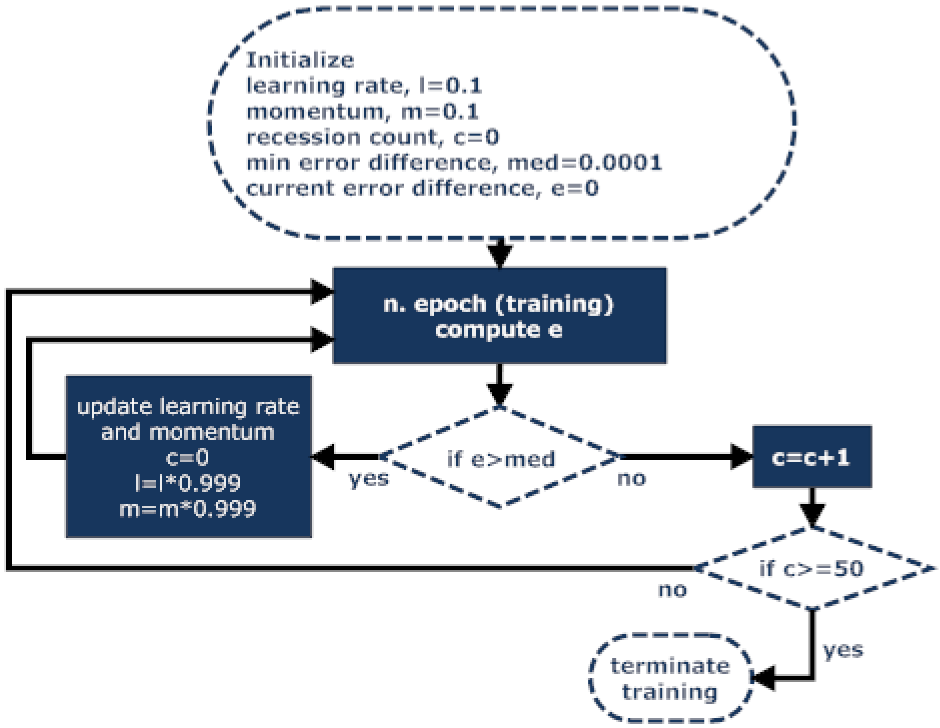

763

764 Figure 11

Hyperspectral Bands

	400	410	420	430	440	450	460	470	480	490	500	510	520	530	540	550	560	570	580	590	600	610	620	630	640	650	660	670	680	690	700	710	720
Bins	0	1	1	2	2	0	0	0	0	0	0	1	2	1	5	10	5	0	3	4	1	0	1	2	4	4	3	2	1	1	0	1	1
1		1	1	1	1																		1	1									
2				1	1								1	1		1	1		3	4	1			1	2	1							
3												1	1		5	8	3								1	1						1	1
4																1	1								1	1			1	1			
5																																	
6																										1	1						
7																											2	2					
8																																	
9																																	
10																																	
11																																	
12																																	

Figure 12

Hyperspectral Bands

Bins	400	410	420	430	440	450	460	470	480	490	500	510	550	600
	6	2	8	2	4	0	0	0	1	0	1	0	0	2
1											1			
2		2	2	2	1				1					
3			1											
4														
5	1		2											
6														
7			1											
8			1											
9	1													1
10														
11	3													
12														
13	1													
14														
15			1											1
16					1									
17														
18					2									
19														
20														
21														
22														
23														
24														
25														

Figure 13